# Phase stability, electronic structure and optical properties of indium oxide polytypes

S. Zh. Karazhanov,[1,2] P. Ravindran,[1] P. Vajeeston,[1] A. Ulyashin,[3] T. G. Finstad,[3] and H. Fjellvåg[1]

[1]*Department of Chemistry, University of Oslo, PO Box 1033 Blindern, N-0315, Oslo, Norway*
[2]*Physical-Technical Institute, 2B Mavlyanov St., Tashkent, 700084, Uzbekistan*
[3]*Department of Physics, University of Oslo, PO Box 1048 Blindern, N-0316, Oslo, Norway*

(Dated: January 17, 2007)

Structural phase stability, electronic structure, optical properties, and high-pressure behavior of polytypes of $In_2O_3$ in three space group symmetry $I2_13, Ia\bar{3}$ and $R\bar{3}$ are studied by first-principles density functional calculations. From structural optimization studies lattice and positional parameters have been calculated, which are found to be in good agreement with the corresponding experimental data. $In_2O_3$ of space group symmetry $I2_13$ and $Ia\ \bar{3}$ are shown to undergo a pressure-induced phase transition to IO3 at pressures around 3.83 GPa. From analysis of band structure it is found that $In_2O_3$ of space group symmetry $I2_13$ is indirect band gap semiconductors, while the other phase of space group $Ia\bar{3}$ is direct band gap. The calculated carrier effective masses for all these three phases are compared with available experimental and theoretical values. From charge-density and electron localization function analysis it is found that these phases have dominant ionic bonding. The magnitude of the absorption and reflection coefficients of $In_2O_3$ with space group $Ia\bar{3}$ and $R\bar{3}$ are small in the energy range 0-5 eV, so that these materials can re regarded and classified as transparent.

PACS numbers: 71.15.-m; 71.22.+i
Keywords: $In_2O_3$, transparent oxides

## I. INTRODUCTION

Transparent conducting oxides (TCO) have risen scientific interest because of their many useful features such as transparency in the visible spectrum of incident light and high electrical conductivity. Interest to investigation of TCO is because of their extensive applications for window layers in solar cells, sensors, front electrodes in flat panel displays, low emissive windows, electrochromic materials in rare-view mirrors of automobiles, smart windows, oven windows, defrosting windows in refrigerators and airplanes, security circuits, holographic recording media, memory chips etc. Investigations on TCO had lead to forming of a new field in optoelectronic device technology, the so-called Transparent electronics or Invisible Electronics.[1–7] Here a combination of the n- and p-type homo p-n junction based on TCO could lead to a functional window, which transmits visible portion of solar radiation, but generates electricity by the absorption of the ultraviolet (UV) part of sunlight.[3]

One of the materials widely used TCO is Sn doped $In_2O_3$ (commonly referred to as ITO). $In_2O_3$ can exist in three different phases characterized by space group symmetries $I2_13, Ia\bar{3}$ and $R\bar{3}$. Among them the bixbyite phase with space group $I2_13$ is rarely studied. Only a few papers[8] are available on crystal structure studies of the phase. The other bixbyite phase of space group $Ia\bar{3}$ with band gap $E_g = 3.7$ eV (Ref. 9) is widely studied both theoretically and experimentally. Until recently, the phase of space group $R\bar{3}$ was also rarely studied because it is a high pressure phase and therefore not easily available. However, recent works have changed this situation. Nanoparticles of $In_2O_3$ in rhombohedral structure have been synthesized by hydrothermal method, followed by post annealing at moderate temperatures and pressures.[10] Phase selective growth of this phase was also demonstrated[11] by means of metal organic chemical vapor deposition (MOCVD) method at high substrate temperatures ($>$ 550 °C) and low (>4 ($\mu$mol/min)) trimethylindium flow rates. Furthermore, it is found[12] that this phase can be formed upon annealing in air at >550 °C of the amorphous indium zinc oxide.

It is well known that upon doping with Sn the conductivity of $In_2O_3$ increases. ITO is widely used for liquid crystal displays and solar cells because of its low electrical resistivity, transparency in the visible spectrum of the solar radiation, compatibility with the patterning processes, and possibility to fabricate at relatively lower temperatures compared to other TCO materials like $SnO_2$ and ZnO. Recently, high-mobility $In_2O_3$ thin film on glass have been identified by doping with transition metals such as Mo[13] and Ti.[14] Heteroepitaxial $In_2O_3$ layers with high carrier mobility of 110 $cm^2/(V\ s)$ and carrier concentration of $6.6\times10^{18}$ $cm^{-3}$ have been obtained by pulsed-laser-deposition method.[15] Commercial ITO films are deposited by magnetron sputtering methods. Currently, research effort is directed toward further decreasing the resistivity to around $1 \times 10^{-4}$ $\Omega$ cm.

From first-principles calculations of the electronic structure of ideal and defective $In_2O_3$ with oxygen vacancies by the discrete variational $X\alpha$ method it is found[9] that vacancy levels appear in the band gap. From comparative analysis of electronic structure for $In_2O_3$, ZnO and $SnO_2$ it was shown that these compounds posses a unique feature as to holes are heavier then conduction band (CB) electrons.[16] *Ab initio* studies of $In_2X_3$ ($X$=O, S, Se, Te) using the tight-binding linear muffin-tin orbital (TB LMTO) method show that compression of the lat-

tice increases the band gap. *Ab initio* studies[17] using the minimum basis sets of the LMTO within the atomic sphere approximation (ASA) has been applied to analyze the X-ray photoelectron, bremsstrahlung isochromat, and optical spectra of $In_2O_3$ and ITO. Based on band structure calculations for $In_2O_3$ and ITO[18,19] using the density functional full-potential (FP) LMTO and full-potential linearized augmented plane wave (FLAPW) method, criteria for transparent conducting behavior has been formulated and it is found that position, dispersion, and character of the lowest conduction band are responsible for electro-optical properties. Studies[20] of the electric-field gradient (EFG) tensor around Cd impurities in $In_2O_3$ by FLAPW method allowed to understand that EFG at the Cd site is accurate and it cannot be described by the point-charge model and antishielding factors. From first-principles molecular orbital calculations native donors such as the oxygen vacancy ($V_O$), In interstitial ($In_i$) and the $V_O$-$In_i$ complex were studied[21] in undoped $In_2O_3$ and it is found that $In_i$ generates a shallow donor level, $V_O$-$In_i$ creates even shallower level, while $V_O$ forms a very deep donor level and facilitate emergence of $In_i$.

Schematic energy band model for ITO was constructed[22] based on x-ray photoelectron spectroscopy (XPS) studies. A systematic study of the electronic structure, as well as optical and transport properties of cubic indium tin oxide was performed[23–25] using the *ab initio* software CRYSTAL. Dependence of carrier mobility and film resistance on carrier concentration in the range $10^{18}$–$10^{22}$ $cm^{-3}$ (Ref. 24), optical spectra in the energy range 0.0–3.1 eV (Ref. 25) and carrier concentrations $10^{18}$–$10^{22}$ $cm^{-3}$ (Ref. 23) were analyzed and good agreement with experimental data was achieved. The electronic band structure and the cohesive energies of $In_4Sn_3O_{12}$ and $In_5SnSbO_{12}$ was calculated by density-functional theory (DFT) within generalized gradient approximations (GGA) and it is found[26] that incorporation of Sb into the $In_4Sn_3O_{12}$ matrix broadens the conduction band.

There still exist some points, which should be clarified: (i) Among the $In_2O_3$ phases of space groups $I2_13, Ia\bar{3}$ and $R\bar{3}$, which we refer to throughout the paper as phase -I, -II, and -III, respectively, only the second one is widely studies; (ii) there is inconsistency in the question as to whether the band gap of $In_2O_3$-II is direct or indirect; (iii) charge density, Bader and Voronoi charge as well as electron localization function analysis were not performed; (iv) structural properties of the $In_2O_3$-I, -II, and -III and possibility of phase transition between these phases were not studied, (iv) optical spectra are available only for films, and $In_2O_3$-II and -III in the narrow energy range 0–6 eV. There are no experimental optical spectra and effective masses for $In_2O_3$-I and -III. The aim of this paper is to study structural, electronic and optical properties of $In_2O_3$-I, -II, and -III by *ab initio* calculations.

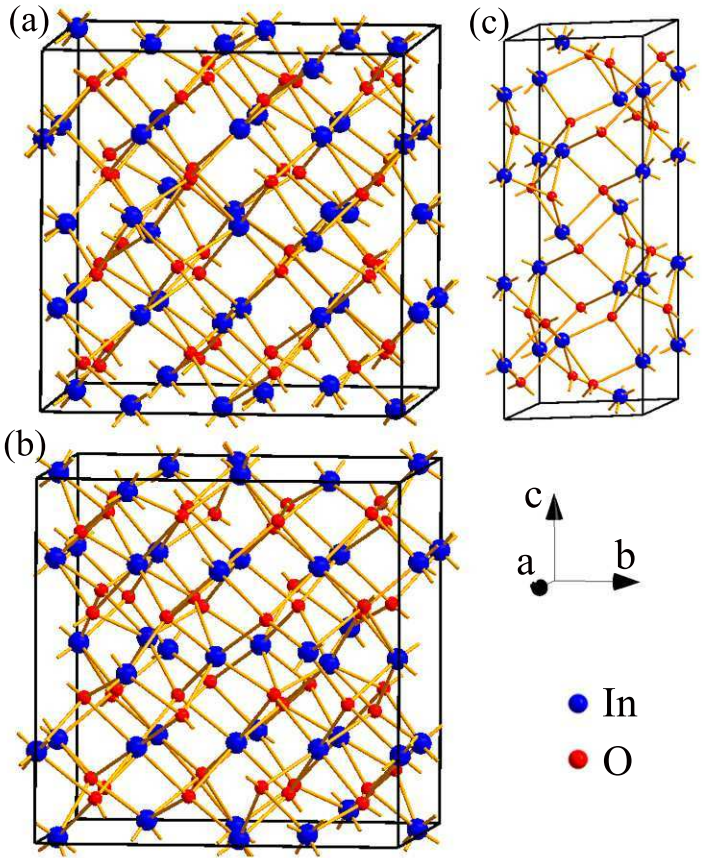


FIG. 1: Crystal structures of (a) $In_2O_3$-I, (b)$In_2O_3$-II, and $In_2O_3$-III.

## II. STRUCTURAL ASPECTS AND COMPUTATIONAL DETAILS

### A. Crystal structures

Crystal structures (Fig. 1) and lattice parameters (Table I) for $In_2O_3$-I, -II, and -III taken from Ref. 27 are used in the present *ab initio* calculations. In all the three polymorphs the coordination is sixfold for In atoms and fourfold for O atoms.

$In_2O_3$-I crystallizes in a cubic bixbyite-type structure (space group number 199) with eight formula units containing three types of In and two types of O atoms occupying 8*a*, 12*b*, 12*b*, 24*c*, and 24*c* Wyckoff positions, respectively. The $In_2O_3$-II phase also crystallizes in a cubic bixbyite-type structure with space group number 206 and eight formula units. Distinct from $In_2O_3$-I, it has different atomic arrangements, bond lengths, and consists of two types of In and one type of O atoms located at Wyckoff positions 8*b*, 24*d*, and 48*e*, respectively. $In_2O_3$-III is of corundum structure with two formula units (space group number 167). It consists of one type of In and one type of O atoms occupying 12*c* and 18*e* Wyckoff posi-

TABLE I: Primitive unit-cell dimensions and volumes, structural parameters, bulk modulus ($B_0$), as well as the derivative of bulk modulus ($B_0'$) for different phases of $In_2O_3$ derived from the present DFT calculations by a search of the total energy minimum. Values given in parentheses refer to experimental data.[27]

| Compound Space group | Unit Cell (Å) | Atom | Site | x | y | z | $B_0$ (GPa) | $B_0'$ |
|---|---|---|---|---|---|---|---|---|
| $In_2O_3$-I | $a$=10.080(10.120)[b] | In1 | 8$a$ | 0.2500(0.2500) | 0.2500(0.2500) | 0.2500(0.2500) | 172.44 | 4.79 |
| $I2_13$ | $b$=10.080(10.120)[b] | In2 | 12$b$ | 0.0335(0.0210) | 0.0000(0.0000) | 0.2500(0.2500) | | |
| | $c$=10.080(10.120)[b] | In3 | 12$b$ | 0.5338(0.5420) | 0.0000(0.0000) | 0.2500(0.2500) | | |
| | $V$=1024.26(1036.43)[b] Å$^3$ | O1 | 24$c$ | 0.1182(0.1250) | 0.1099(0.1350) | 0.3456(0.3950) | | |
| | | O2 | 24$c$ | 0.1543(0.1000) | 0.3821(0.3580) | 0.3901(0.3730) | | |
| $In_2O_3$-II | $a$=10.077(10.117)[a] | In1 | 8$b$ | 0.2500(0.2500) | 0.2500(0.2500) | 0.2500(0.2500) | 172.87 | 4.75 |
| $Ia\bar{3}$ | $b$=10.077(10.117)[a] | In2 | 24$d$ | 0.4665(0.4668) | 0.0000(0.0000) | 0.2500(0.2500) | | |
| | $c$=10.077(10.117)[a] | O | 48$e$ | 0.3900(0.3905) | 0.1544(0.1529) | 0.3820(0.3832) | | |
| | $V$=1023.28(1035.51)[a] Å$^3$ | | | | | | | |
| $In_2O_3$-III | $a$=5.4928(5.4870)[c] | In | 12$c$ | 0.0000(0.0000) | 0.0000(0.0000) | 0.3576(0.3573) | 183.61 | 4.62 |
| $R\bar{3}c$ | $b$=5.4928(5.4870)[c] | O | 18$e$ | 0.2961(0.2980) | 0.0000(0.0000) | 0.2500(0.25000) | | |
| | $c$=14.4242(14.5100)[c] | | | | | | | |
| | $V$=376.89(378.33)[c] Å$^3$ | | | | | | | |

[a]Experimental values from Ref. 28.
[b]Experimental values from Ref. 8.
[c]Experimental values from Ref. 10,29.

tions, respectively. This is a high pressure phase[10] and consequently has been rarely produced, but it has been claimed[10,11] that the some properties, especially the stability of the conductivity should be favorable to material of the cubic structures.

### B. Density-functional calculations

The band-structure calculations have been performed using the VASP-PAW package,[30] which calculates the Kohn–Sham eigenvalues in the framework of the DFT[31] within the local density (LDA) and GGA.[32] The exchange and correlation energy per electron were described by the Perdew-Zunger parametrization[33] of the quantum Monte Carlo results of Ceperley-Alder.[34] The interaction between electrons and atomic cores was described by means of non-norm-conserving pseudopotentials implemented in the VASP package. The pseudopotentials are generated in accordance with the projector-augmented wave (PAW) method.[35,36] The use of the PAW pseudopotentials addresses the problem of the inadequate description of the wave functions in the core region - a problem common to all pseudopotential approaches.[37] The application of the pseudopotentials allow us to construct orthonormalized all-electron-like wave functions for the In-4$d$ and -5$s$, and O-2$s$ and -2$p$ valence electrons. Spin-orbit coupling was not included in the present calculations.

The diagonal elements of the effective mass tensor for the conduction band (CB) electrons are calculated by:

$$\frac{1}{m_c(\mathbf{k})} = \frac{1}{h^2}\frac{\partial^2 E(\mathbf{k})}{\partial \mathbf{k}^2} \tag{1}$$

for a direction $\mathbf{k}$ in $\mathbf{k}$ space from the $\Gamma$ point towards the other high-symmetry points in the Brillouin zone of $In_2O_3$-I, -II, and -III. We use this to give an indication of the conduction, since the CB minimum of the band dispersions of all the compounds considered [see Sec. III B] are located at the $\Gamma$ point of the Brillouin zone. The band edge energies $E(\mathbf{k})$ have been extracted from DFT calculations and 9th order polynomial fitting has been performed. From the polynomial second order derivative was calculated, which was used in the effective mass calculations by Eq. 1. We studied the effective masses along [001], [011] and [111] corresponding to the directions $\Gamma \rightarrow H, \Gamma \rightarrow N$, and $\Gamma \rightarrow P$, respectively, for $In_2O_3$-I and -II, $\Gamma \rightarrow L, \Gamma \rightarrow F$, and $\Gamma \rightarrow Z$ for $In_2O_3$-III.

The equilibrium lattice parameters and bulk modulus of $In_2O_3$-I, -II, and -III are determined by a total energy calculation and fitted into the Birch-Murnaghan equation of state. The calculations have been performed on a $\Gamma$ centered 10×10×10 k-grid in the entire Brillouin zone.

### C. Optical properties

The imaginary part of the optical dielectric function $\epsilon_2(\omega)$ has been derived from DFT results by summing transitions from occupied to unoccupied states for energies much larger than those of the phonons:

$$\epsilon_2^{ij}(\omega) = \frac{Ve^2}{2\pi\hbar m^2\omega^2}\int d^3\mathbf{k}\sum_{nn'}\langle\mathbf{kn}|p_i|\mathbf{kn'}\rangle\langle\mathbf{kn'}|p_j|\mathbf{kn}\rangle \times f_{\mathbf{kn}}(1-f_{\mathbf{kn'}})\delta(\epsilon_{\mathbf{kn'}}-\epsilon_{\mathbf{kn}}-\hbar\omega). \tag{2}$$

Here $(p_x, p_y, p_z) = p$ is the momentum operator, $f_{\mathbf{kn}}$ is the Fermi distribution, and $|\mathbf{kn}\rangle$ is the crystal wave function, corresponding to the energy $\epsilon_{\mathbf{kn}}$ with momentum $\mathbf{k}$.

The real part of the dielectric function $\epsilon_1(\omega)$ is calculated using the Kramer–Kronig transformation. The knowledge of both the real and imaginary parts of the dielectric tensor allows one to calculate other important optical parameters. In this paper we present and analyze

the reflectivity $R(\omega)$, the absorption coefficient $\alpha(\omega)$, the refractive index $n(\omega)$, and the extinction coefficient $k(\omega)$:

$$R(\omega) = \left| \frac{\sqrt{\epsilon(\omega)} - 1}{\sqrt{\epsilon(\omega)} + 1} \right|^2, \quad (3)$$

$$\alpha(\omega) = \omega \sqrt{2\sqrt{\epsilon_1^2(\omega) + \epsilon_2^2(\omega)} - 2\epsilon_1(\omega)}, \quad (4)$$

$$n(\omega) = \sqrt{\frac{\sqrt{\epsilon_1^2(\omega) + \epsilon_2^2(\omega)} + \epsilon_1(\omega)}{2}}, \quad (5)$$

$$k(\omega) = \sqrt{\frac{\sqrt{\epsilon_1^2(\omega) + \epsilon_2^2(\omega)} - \epsilon_1(\omega)}{2}}. \quad (6)$$

Here $\epsilon(\omega) = \epsilon_1(\omega) + i\epsilon_2(\omega)$ is the complex dielectric function. The calculated optical parameters have more spectral structure[38–41] than what is commonly observed because no fluctuations are included. To facilitate comparison with experimental data, the calculated optical spectra is smoothed by broadening. The exact form of the broadening function is unknown. Also, the instrumental resolution smears out many fine features. These features have been modelled using the lifetime broadening technique by convoluting the imaginary part of the dielectric function with a Lorentzian with a full width at half maximum of $0.002(\hbar\omega)^2$ eV and increasing quadratically with the photon energy.

For simplification of the presentation of the findings, the labels $E_0, E_1, E_2, d_1$, and $d_2$ of Ref. 42 (from the reflectivity spectra) used for semiconductors of wurtzite and zinc blende structure were retained. The subscript 0 in $E$ refers to transitions occurring at $\Gamma$, 1 for transitions at points in the [111] direction and 2 for transitions at points in the [100] direction of the $\mathbf{k}$ space.[42]

## III. RESULTS AND DISCUSSION

### A. Ground-state properties

Using the experimentally determined crystal information as input, structural optimization has been performed for $In_2O_3$-I, -II, and -III by the following procedure: first, atomic positions have been relaxed by force minimization method keeping the volume and shape of the crystal fixed. Using the relaxed atomic positions as input, the crystal volume and shape have been relaxed using stress minimization freezing out atomic positions. Then these optimized parameters have been used as input to relax atomic positions, cell volume and shape altogether. Crystal structure information obtained by this way was used as input for calculation of the total energy ($E_{\rm tot}$) as a function of the cell volume ($V$). The minima $E_{\rm tot}^{\rm min}$ of the dependence $E_{\rm tot}(V)$ are taken as the equilibrium volume. Positional and lattice parameters derived from the DFT calculations for the equilibrium lattices are given in Table I together with experimentally determined values. Analysis of the Table I shows that deviation of the calculated equilibrium volumes are $< 1.2$ % of the experimentally determined values, which indicates that the theoretical calculations are reliable to predict structural parameters for such complex systems. Furthermore, symmetry of the thus optimized lattices is checked for $In_2O_3$-I, -II, and -III and it is found that it is the same as that of the experimentally determined one. Although for the $In_2O_3$ phases studied in this paper the calculated and experimentally determined lattice parameters do not deviate much from each other, such a structural study is still needed because for some compounds, e.g., $KAlH_4$ (Ref. 43) they may differ and can also lead to revealing of a new phase of a solid, e.g., (Ref. 44), which are not yet observed experimentally.

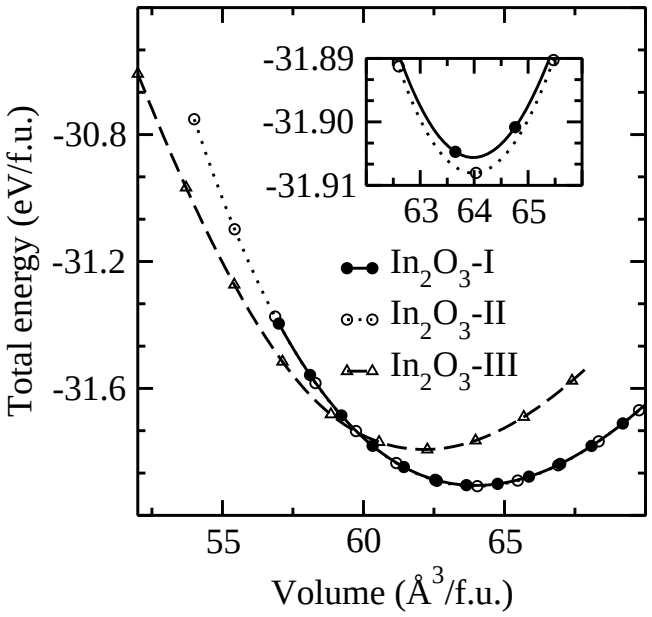


FIG. 2: Dependence of total energy $E_{\rm tot}$ on cell volume $V$ per formula unit for $In_2O_3$-I , $In_2O_3$-II, and $In_2O_3$-III. Magnified version of the dependence $E_{\rm tot}(V)$ for $In_2O_3$-I and -II around $E_{\rm tot}^{\rm min}$ is shown in the inset.

Analysis of Fig. 2 shows that $E_{\rm tot}^{\rm min}$ for $In_2O_3$-III is larger than that of $In_2O_3$-I and -II. Consequently, $In_2O_3$-III is less stable than $In_2O_3$-I and -II. Total energies and equilibrium volumes for $In_2O_3$-I and -II are nearly the same at the equilibrium and these two phases coexist in a certain volume range. Not only total energies are nearly the same, but also crystal structures of $In_2O_3$-I and -II are closely related [Fig. 1]. Difference between these two phases is in the Wyckoff sites for the In and O atoms, positional parameters, and, consequently the space group symmetry of the phases [Table I].

In the Fig. 2 it is seen that the total energy values for $In_2O_3$-I and -II are almost the same. In the insert to Fig. 2 a magnified version of the dependence $E_{\rm tot}(V)$ is presented in the close vicinity of $E_{\rm tot}^{\rm min}$. From the inset it is seen that the total energy minimum and equilibrium volume for $In_2O_3$-II is lower than that of $In_2O_3$-I. Consequently, $In_2O_3$-II is the most stable phase compared

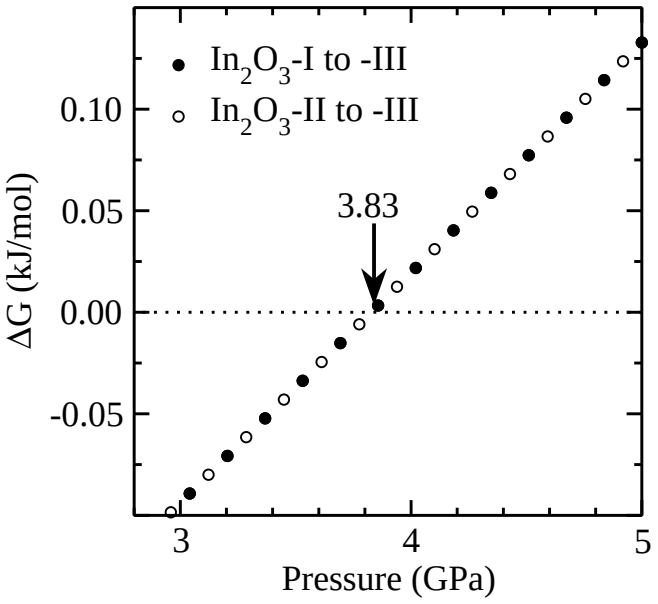


FIG. 3: Gibbs free-energy difference relative to $In_2O_3$-I (closed circles) and to -II (open circles) as a function of the applied pressure. Transition point is marked with an arrow and numerical pressure value (in GPa) is stated.

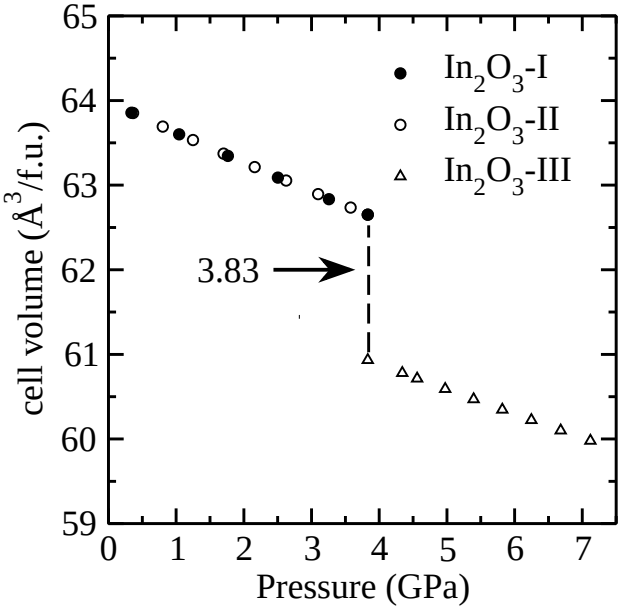


FIG. 4: Calculated cell volume as a function of pressure for $In_2O_3$-I, -II, and -III. Transition point is marked with an arrow and pressure value at the transition point (in GPa) is stated.

to $In_2O_3$-I and -III. Furthermore, at lower volumes, and, respectively, higher pressures, the dependence $E_{\rm tot}(V)$ for $In_2O_3$-III crosses that for $In_2O_3$-I and II. It indicates that upon compression $In_2O_3$-I and II can transformed into $In_2O_3$-III. In order to estimate the pressure value for the transitions $In_2O_3$-I to -III and $In_2O_3$-II to -III, we have plotted dependence of the Gibbs free-energy difference ($\Delta G$) as a function of the applied pressure ($P$) [Fig. 3]. Since equilibrium volumes and total energy minimums for $In_2O_3$-I and -II are nearly the same, the dependencies $\Delta G(P)$ for the transition $In_2O_3$-I to -III and $In_2O_3$-II to -III coincide. The pressure value at which $\Delta G = 0$ is the one required for the structural phase transition. According to our findings in Fig. 3 the pressure induced phase transitions from $In_2O_3$-I to -III and from $In_2O_3$-II to -III occur at $P = 3.83$ GPa.

The pressure-induced structural transition is well demonstrated in dependence of the cell volume on applied pressure [Fig. 4]. It is seen that the volume shrinkage at the transition pressure is 1.719 Å$^3$. The phase transitions $In_2O_3$-I-to-III and $In_2O_3$-II-to-III are accompanied by breaking and transformations of chemical bonding between atoms and reconstruction of anion and cation sublattices.

Phase transition from $In_2O_3$-II to -III was studied experimentally in the literature before. The calculated transition pressure value differs from experimental data. In Ref. 45 such a transition has been demonstrated experimentally[45] at 6.5 GPa and 1250 $^o$C. However, at pressures up to 6 GPa and temperatures 550, 1000, and 1450 $^o$C $In_2O_3$ retained[46] in phase -II. According to experiments of Ref. 29 mixture of $In_2O_3$ with Co posses the same structure as $In_2O_3$-III. In other experiments of Ref. 29 with pure $In_2O_3$ formation of $In_2O_3$-III was possible at 800 $^o$C provided if the sample is initially preheated 1250 $^o$C. Without the preheating, formation of $In_2O_3$-III occurred at 1000 $^o$C only. Distinct from Ref. 29,45 and 46 the pressure-induced phase transition reported in the present work correspond to 0 K. The phase selective growth of $In_2O_3$-III in the experiments of Ref. 11 the pressure was always very low (20 kPa).

Bulk modulus is the parameter characterizing compressibility of a solid. The calculated bulk modulus for $In_2O_3$-I and -II are nearly the same, because equilibrium volumes and total energy minimums of the $In_2O_3$ phases are almost the same. However, bulk modulus of $In_2O_3$-III is larger than that for $In_2O_3$-I and -II. Consequently, the latter are more easily compressible than $In_2O_3$-III. There are no experimental data on bulk modulus of pure $In_2O_3$-I, -II, and -III. So, the calculated bulk modulus have been compared to 99±32 GPa of ITO films.[47] It is seen that our data [Table I] is much larger than that of the ITO films and consequently, are hardly compressible than the Sn doped $In_2O_3$ films.

### B. Band structure

For a better understanding about electronic-, optical-properties, and chemical bonding of the poly-types of indium oxide, band structures can be quite helpful. Band structures for $In_2O_3$-I, -II, and -III calculated in the present work are presented in Fig. 5. Although all these phases are different, they have some similar features. The

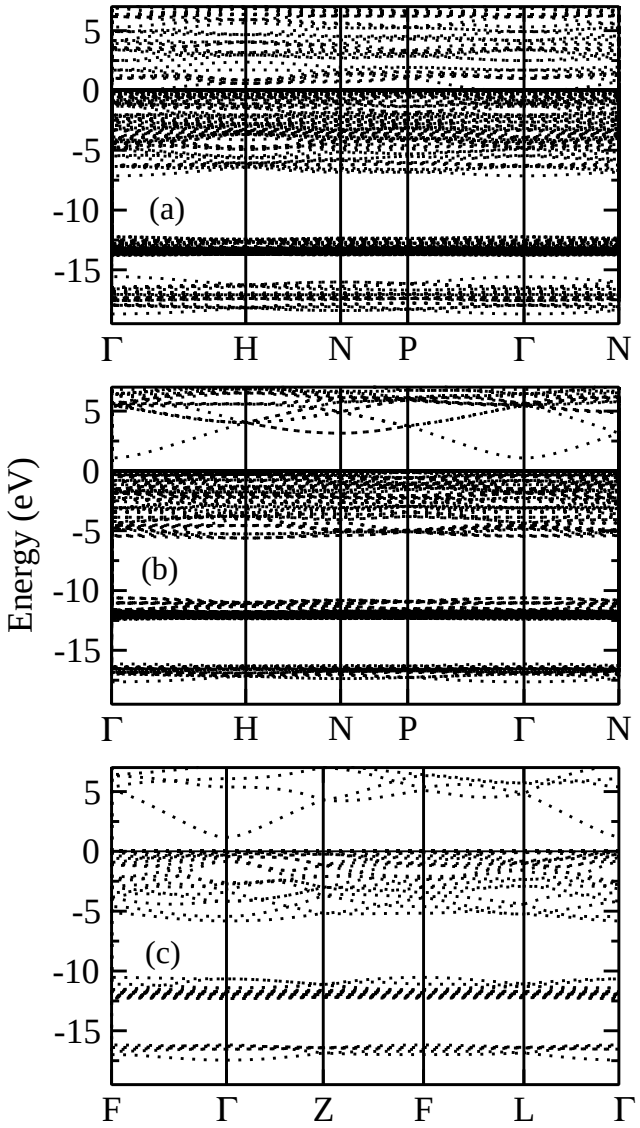


FIG. 5: Band dispersion for (a) $In_2O_3$-I, (b) $In_2O_3$-II, and (c) $In_2O_3$-III at the equilibrium volume. The Fermi level is at the topmost VB and it is set to zero.

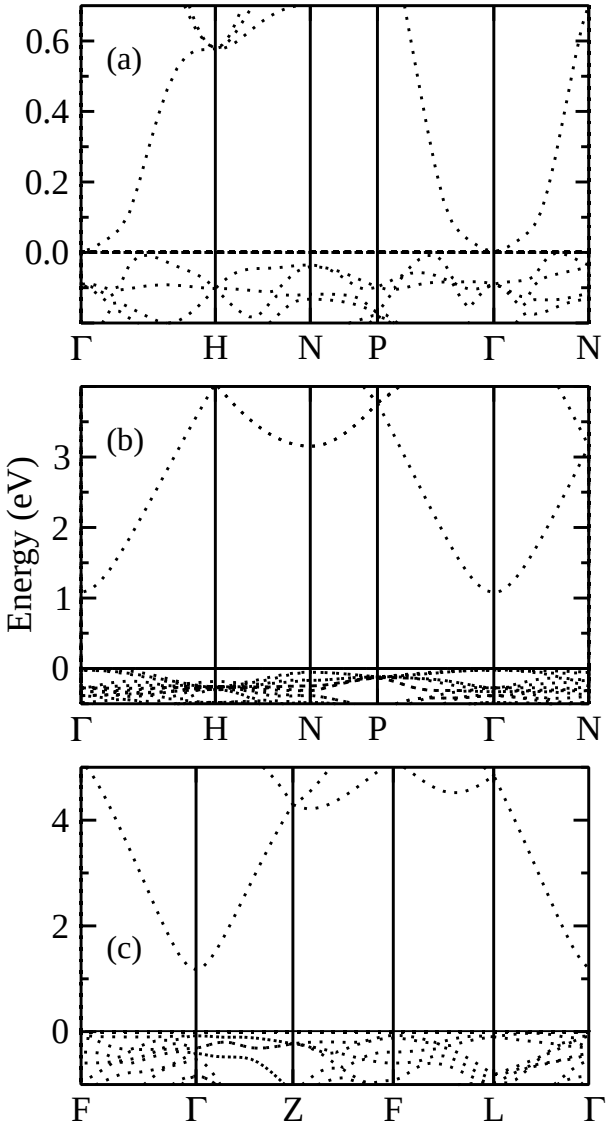


FIG. 6: Band structure for (a) $In_2O_3$-I, (b) $In_2O_3$-II, and (c) $In_2O_3$-III near the VB maximum and CB minimum. The Fermi level is set to zero.

valence band (VB) consists of three regions in all the three phases. The lowest one is located below −15 eV from the topmost VB. The bands at the intermediate energy region is located between −14 and −10 eV. Both of the bands are well localized, while the topmost band is quite broad.

An interesting feature in the band structure of the $In_2O_3$ phases is that the bottommost CB is dispersive and is located at the Γ point, while the topmost VB is flat, which are the important properties inherent to TCO materials. The bands at the topmost VB of the $In_2O_3$ phases are very close to each other [Fig. 5] and hence it is hard for the eye to identify the maximum in the VB. In order to have more detailed information about the topmost VB the electronic structure is plotted for narrower energy range around the band gap [Fig. 6]. From this figure it is clear that CB minimum is located at the Γ point for all structures and the VB maximum is located in between Γ−H, Γ−P, and Γ−N points for $In_2O_3$-I and at the Γ point for $In_2O_3$-II. It is flat for $In_2O_3$-III. Consequently, one can conclude that $In_2O_3$-I is indirect gap, while $In_2O_3$-II is direct gap material.

The direct band gaps coming out from the LDA calculations are presented in Table II along with the experimentally determined values. Analysis of the Table II shows that band gaps for $In_2O_3$-II and -III are drastically underestimated due to the well-known problem of the DFT in calculated band gaps. Experimental data for the band gap for $In_2O_3$-I is not yet available. Our calculated band gap for $In_2O_3$-II is in good agreement with 0.9 eV,[16] 1.0 eV,[18] and < 1.0 eV,[17] determined from DFT calculations. Optical band gap of $In_2O_3$-III is found to

be larger than that of $In_2O_3$-I and -II. So, one can expect from $In_2O_3$-III transparency in wider energy range of the optical spectra than the other from $In_2O_3$ phases.

TABLE II: Optical (in brackets) and fundamental band gaps (in eV) for $In_2O_3$-I, -II, and -III calculated by DFT within LDA ($E_g^{\rm LDA}$)and GGA ($E_g^{\rm GGA}$) using the lattice parameters determined theoretically ($a_0$) and experimentally ($a_e$) along with experimentally measured ones ($E_g^{\rm Expt}$).

| Phase | $E_g^{\rm LDA}$ | | $E_g^{\rm GGA}$ | | $E_g^{\rm Expt}$ |
|---|---|---|---|---|---|
| | $a_0$ | $a_e$ | $a_0$ | $a_e$ | |
| $In_2O_3$-I | | 0.09 | | | |
| $In_2O_3$-II | 1.17 | 1.10 | 1.33 | 1.29 | 3.70 (Ref. 9) |
| | (2.08) | (2.08) | (2.02) | (2.06) | 3.60 (Ref. 48) |
| | | | | | 3.70 (Ref. 11) |
| $In_2O_3$-III | | 1.25 | | | 3.80 (Ref. 29) |
| | | (3.12) | | | 3.00 (Ref. 11) |

The band gap is an important parameter for characterization of TCO materials. From room temperature fundamental absorption edge studies it was found[49] that direct and indirect band gaps of single crystal $In_2O_3$-II are 3.750 and 2.619 eV, respectively. Similar band gap values have been found[50] from absorption measurements for $In_2O_3$ films which decreased with increasing film thickness from 2.65 eV for 100 nm to 2.40 eV for 400 nm. The band gap decreased also with increasing deposition temperature from 2.50 eV at 20 K to 2.30 eV at 270 K. Band gap reduction from 2.46 eV to 2.30 eV was caused also by increase of the annealing temperature from 200 to 500 K. Theoretical studies of band structure of $In_2O_3$-II still remains controversial. By band structure calculations using the LMTO method within the atomic sphere approximation (ASA) based on the LDA it is found[17] that the band gap of $In_2O_3$-II is indirect with CB minimum at the Γ point and VB maximum at H point. The energy difference of the topmost VB at the Γ and $H$ points was 0.072 eV, which is too small compared to experimentally determined one 1.13 eV. However, DFT calculations of Refs. 16,18,51 show that the band gap of $In_2O_3$-II is direct with CB minimum and VB maximum located at Γ point. The band gap 1.0 eV was found for experimental lattice constant and 1.5 eV for theoretically determined lattice constants.[18] Our results are in agreement with these findings. Figure 7 presents band structure of $In_2O_3$-II calculated using the theoretically and experimentally determined lattice constants within LDA and GGA. It is seen that the CB minimum and VB maximum are located at the Γ point. Hence we conclude that the band gap of $In_2O_3$-II is direct.

Comparative analysis of band structures for $In_2O_3$-I and -II [Fig. 6 (a) and (b)] shows that electronic structure of these two phases differ each from other drastically despite equal number of atoms in the unit cell. The difference is caused by atomic arrangement and bond lengths. Furthermore, it seems that the band of $In_2O_3$-I [Fig. 5 (a)] located right up the Fermi level is split from the other CB states. To get more insight into the CB

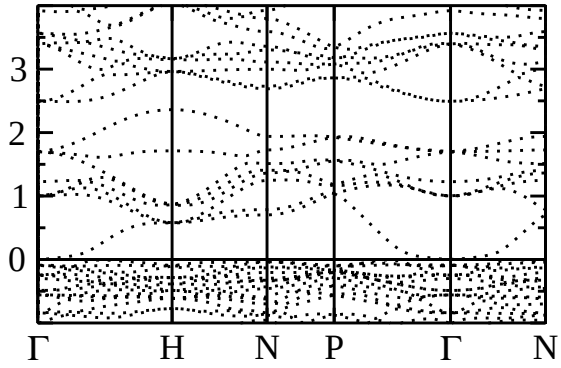


FIG. 7: Band structure for $In_2O_3$-II calculated within (a) LDA for the theoretically determined lattice constant and GGA for the (b) theoretically and (c) experimentally determined lattice parameters. The Fermi level is set to zero.

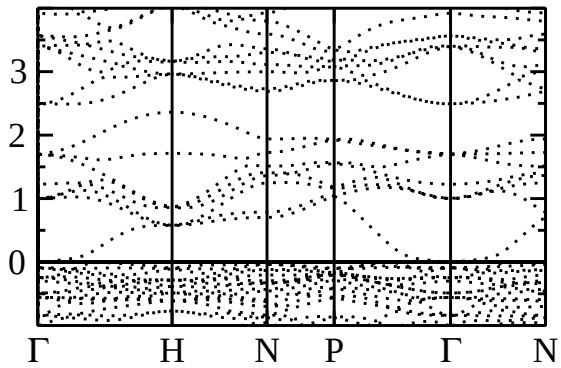


FIG. 8: CB for $In_2O_3$-I in a more extended energy scale near the Fermi level set to zero.

spectra near $E_F$, we plot the band structure for $In_2O_3$-I in a more expanded energy scale in Fig. 8. In this figure, it is seen that the band is more or less split from the other CB's. So, it can be called an intermediate band (IB) formed by changes in atomic arrangements and bond lengths. Since the band is highly dispersive, recombination of electrons and holes through the band is not expected to be very high. Width of the band is 2.4 eV. There are no electrons in the band. So, it can be useful for photoemission of electrons from VB to the IB. In the DFT calculations the VB to IB optical transition is expected to be very intensive because of the underestimation of the band gap. It is demonstrated in the studies of optical spectra of the $In_2O_3$ phases of this paper.

### C. Density of states

To explore the origin of the VB and CB of $In_2O_3$-I, -II, and -III density of states (DOS) has been analyzed. In Fig. 9 presents total DOS has been compared to XPS, bremsstrahlung isochromat spectroscopy (BIS), soft x-ray emission (SXE), and soft x-ray absorption spectroscopy (SXA) measurements. The DOS ex-

hibit sharper peaks than the experimental spectra, since we have not included the lifetime broadening and instrumental resolution. As noted in Introduction, there are no experimental data on XPS studies of $In_2O_3$-I. So, comparison with experimental data shall be performed for the $In_2O_3$-II and -III phases.

As noted in the previous section, there are three distinct regions in the VB of the $In_2O_3$ phases considered in the present work. According to the band dispersion and total DOS analysis width of the bands are 2.22, 1.52, and 6.38 eV for $In_2O_3$-I, 1.5, 1.77, and 5.46 for $In_2O_3$-II, and 0.81, 1.74, and 5.5 eV for $In_2O_3$-III. These results are in fair agreement with that of Ref. 16, which from DFT calculations found 2.33 eV for the middle band and 5.70 eV for the topmost valence band. The discrepancy can be related to approximations and methods used in the calculations.

It is seen from Fig. 9(a) that intensity of the lowest VB of $In_2O_3$-I is much smaller and its width is larger than those of $In_2O_3$-II and -III. Furthermore, the band for $In_2O_3$-I is split into four well-defined sharp peaks. Location of the bands in $In_2O_3$-I, -II, and -III coming out from the DFT calculations is shifted toward higher energies and their intensity are much higher compared to experimental data [Fig. 9(d)].

The next band located at higher energies is well localized. As we found from the orbital and site projected DOS analysis, the band is originated from In 4*d* electrons. In case of $In_2O_3$-I the band is located at lower energies than it is $In_2O_3$-II and -III. Width and intensity of peaks of the topmost VB is more or less the same for $In_2O_3$-I, -II, and -III.

Analysis of the Fig. 9 shows that width of the topmost valence band of $In_2O_3$-I, -II, and -III more or less agrees with SXE measurements, which shows a well-defined intensive peak closer to the topmost VB. Such a peak is not available in other experimental spectra shown in Fig. 9.

In the total DOS for $In_2O_3$-I [Fig. 9 (a)] IB is seen, which is isolated from both CB and the VB. This result is in agreement with band structure analysis [Fig. 8]. There is no such a band in other $In_2O_3$ phases -I and -II.

It should also be noted that there is discrepancy in the XPS results of different groups. For example, binding energy of the In 4*d* band is found to be at 14 eV in Ref. 52 and 18 eV in Ref. 53. Widths of the calculated peaks of the lowest and middle VB regions agree with experimental data of Refs. 52–54. However, the location of the two calculated peaks are shifted toward higher energies compared to experimental data. Furthermore, in our calculations these two peaks are much more intensive than the topmost valence band, which disagrees with the experimental data, but agrees with theoretical calculations of Refs. 9,17. It is worth to note that the pseudocore d-bands are not placed correctly in systems such as ZnO[55] and CdTe[56] by present type of calculations. So, one should go beyond the LDA/GGA calculations by accounting the strong correlation effects from the In 4*d* electrons through LDA+*SIC* method. We believe that

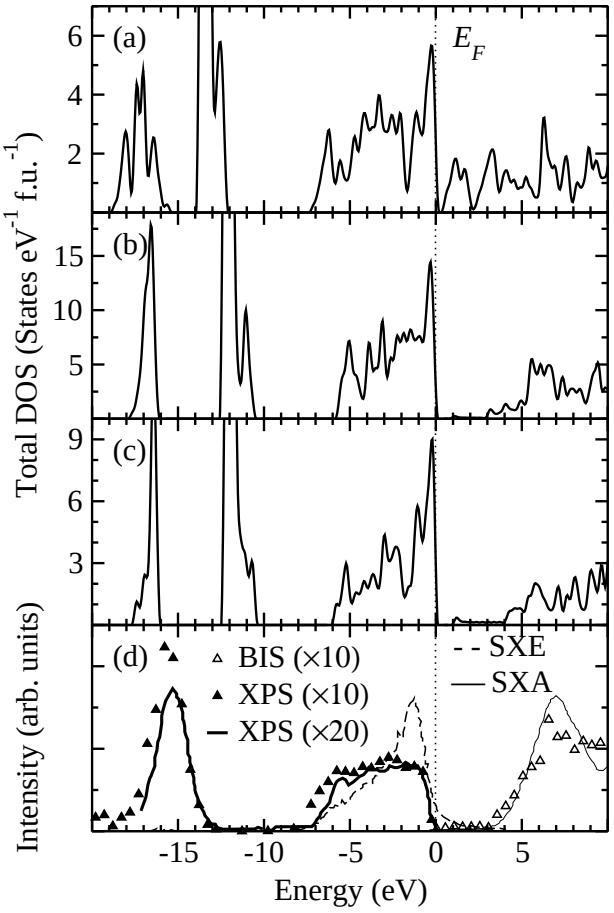


FIG. 9: (a-c) Calculated total DOS for (a) $In_2O_3$-I, (b) -II, and (c) -III as compared with experimental data using different techniques (d) BIS (open triangles),[52] XPS (closed triangles, Ref. 52), XPS (thick solid lines, Ref. 53), SXE,[54] and SXA.[54] The Fermi level is set to zero.

such calculation not only place the In 4*d* states at correct place, but also improve the predicted band gap of indium oxides polytypes.

Insight into the bonding interaction between constituents can be obtained from the site and orbital projected partial DOS analysis. Moreover, analysis of the projected DOS (PDOS) give detailed information about the origin of CB and VB electronic energy levels. Such analysis has been performed for all the phases of $In_2O_3$ considered in the present work [Fig. 10]. The main feature in Fig. 10 is that the DOS distribution of In and O energetically are not separated indicating that nature of chemical bonding is not pure ionic and there is some covalency. It is seen in Fig. 10 that the lowest energy states at the VB are mainly contributed by O-2*s* electrons with noticeable In 4*d* electrons. The VB states around -12 eV are basically from In 4*d* electrons with small contribution from O 2*s* and 2*p* states due to hybridization interaction. The states around −5 eV in the VB are equally contributed by both In 5*s* and O 2*p* electrons. The main contribution to the topmost valence band of $In_2O_3$-I, -II,

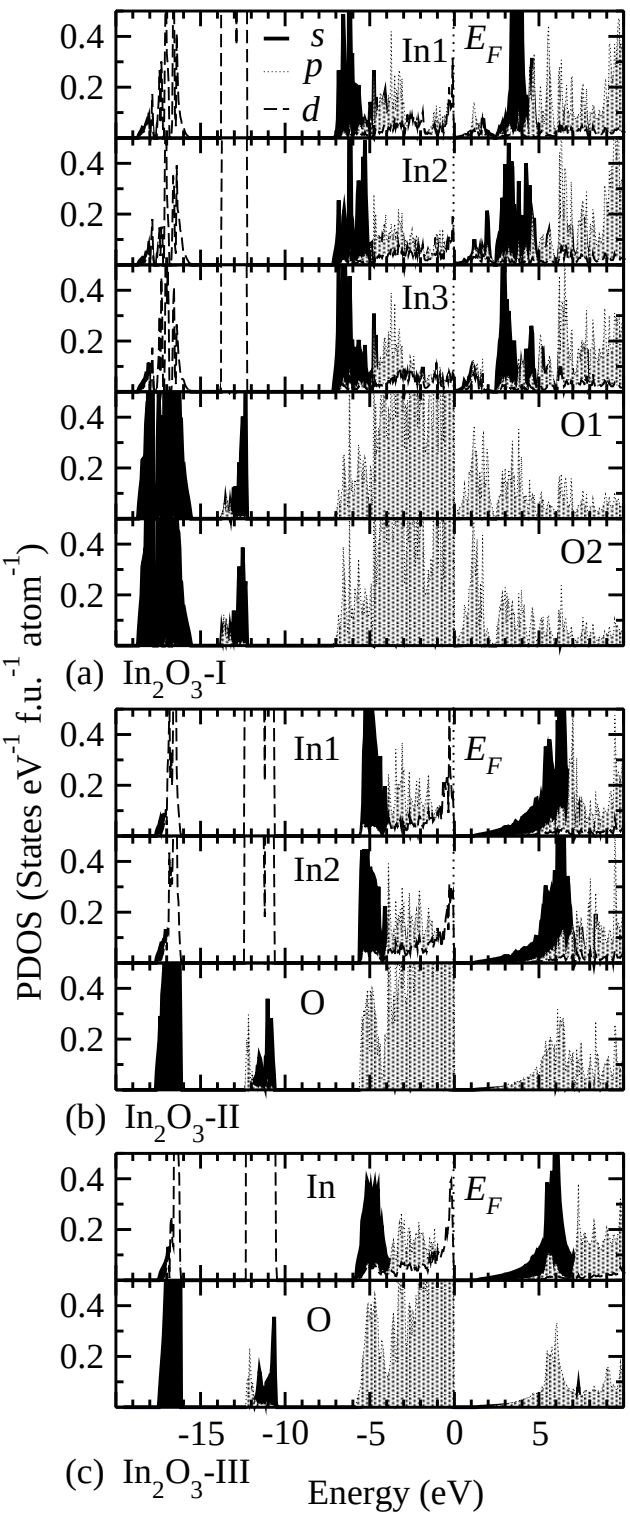


FIG. 10: The orbital and site-projected DOS of (a) $In_2O_3$-I, (b) -II, and (c) -III. The Fermi level is set at zero of energy.

and -III is from O $2p$ electrons which has noticeable hybridization interaction with In $4d$/5p electrons compared with the O 2p states in $In_2O_3$-II and -III, that in $In_2O_3$-I are well dispersed in the VB due to relatively shorter distance between the oxygen atoms and hence increased overlap interaction in this phase. Overall the results from the PDOS analysis are in good agreement with those of previous *ab initio* calculations[9,17,18] and recent SXE and SXA spectra measurements for $In_2O_3$-II. Nature of the topmost VB is similar to that of ZnO (see e.g. Ref. 57).

Analysis of the orbital and site projected DOS shows that the IB of $In_2O_3$-I posses mainly O $2p$ character hybridized with In $5s$ and $4d$ orbitals. CB minimum of $In_2O_3$-I, -II, and -III are mainly originating from In $5s$ hybridized with O $2p$ electrons.

As indicated in Ref. 18 the position, dispersion and character of the lowest CB carry the key features responsible for electro-optic properties of TCO materials. It follows from our orbital and site projected DOS that the IB of $In_2O_3$-I consists mainly of O $2p$ character hybridized with In $5s$ and $4d$ orbitals. The CB minimum of $In_2O_3$-I, -II, and -III are mainly originating from In $5s$ electrons.

Orbital and site decomposition analysis is used for quantitative characterization of the contributions of $s, p_x, p_y, p_z, d_{xy}, d_{xz}, d_{yz}, d_{x^2-y^2}$ and $d_{z^2}$ orbitals into the bands of particular interest. From such analysis it is found that the topmost VB of $In_2O_3$-I, -II, and -III is contributed from O $2p_x, 2p_y, 2p_z$ orbitals which slightly hybridized with In $4d_{xy}, 4d_{xz}, 4d_{yz}$ orbitals.

IB of $In_2O_3$-I is strongly contributed from O $2p_x, 2p_y$ and $2p_z$ orbitals with noticeable effect of In $5s$ and In $4d_{xy}, 4d_{xz}, 4d_{yz}$ orbitals. The origin of the CB minimum of $In_2O_3$-I, -II, and -III is more or less the same and it basically comes from In $5s$ orbitals with small O $2s, 2p_x, 2p_y$, and $2p_z$ character. These results are consistent the conclusions arrived from orbital and site projected DOS [Fig. 10]. Based on this analysis and the basic formulations suggested in Ref. 18 regarding highly dispersed and single character $s$-type band at the bottommost CB the features that favor TCO behavior one can conclude that $In_2O_3$-II posses the feature of $s$-electron based TCO. As noted in our previous publication (Ref. 58) $ZnSiO_3$ and $Zn_2SiO_4$ can also be classified as $s$-electron based TCO. It follows from the above site and orbital decomposed DOS analysis that $In_2O_3$-II and -III do not have the features to classify them neither to $s$ electron nor to $d$ electron based TCO materials such as anatase $Ti_{1-x}Nb_xO_2$ (Ref. 59) and $TiO_2$ (Ref. 60) with dominant $d$ character at the CB minimum.

### D. Conduction band effective masses

Effective masses characterize band dispersion and are one of the important parameters linking electronic structure with transport properties of solids. As noted above, the lowest IB of $In_2O_3$-I, and CB of $In_2O_3$-II, and -III are more dispersive than the topmost VB, which means

that the IB and CB electrons are lighter than holes. Almost flat topmost VB indicates that valence electrons are tightly bound to the atoms. Consequently, the dominating charge carriers in an intrinsic $In_2O_3$ is expected to be electrons and not holes. Here we focus on the IB and CB electron effective masses. The results are presented in Table III. Analysis shows that the calculated masses for $In_2O_3$-I, -II, and -III are almost isotropic. Small anisotropy can be related to the effect of $p$ and $d$ orbitals hybridizing with $s$ orbitals. The deviation in the calculated effective masses is in the range 23–33 % of the experimentally measured one. This underestimation is related to the well-known DFT error. Not only the band gap, but also the band dispersion comes out incorrectly and this effect is well pronounced in transition metal oxides (see, e.g., Ref. 55,56,58,61–66). Experimental data for CB electron effective masses are available for $In_2O_3$-II only. The masses calculated by LMTO ASA (Ref. 17) method agree fairly with experimental data and are more anisotropic than our results.

TABLE III: Calculated effective masses of CB electrons (in units of the free-electron mass $m_0$ and in the directions indicated) for $In_2O_3$-I, -II, and -III are compared with available experimental and calculated values.

| $In_2O_3$-I | $In_2O_3$-II | $In_2O_3$-III | ZnO |
|---|---|---|---|
| 0.23 (Γ-H) | 0.23 (Γ-H) | 0.16 (Γ-F) | 0.23 ($E \parallel c$)[a] |
| 0.23 (Γ-N) | 0.20 (Γ-N) | 0.14 (Γ-L) | 0.21 ($E \perp c$)[a] |
| 0.20 (Γ-P) | 0.23 (Γ-P) | 0.15 (Γ-Z) | 0.24[b] |
| | 0.42 (Γ-H)[c] | | 0.28 ($E \parallel c$)[d] |
| | 0.30 (Γ-N)[c] | | 0.32 ($E \perp c$)[d] |
| | 0.36 (Γ-P)[c] | | 0.14 ($E \parallel c$)[e] |
| | 0.30 (Γ-H)[f] | | 0.13 ($E \perp c$)[e] |
| | 0.36 (Γ-N)[f] | | |
| | 0.41 (Γ-P)[f] | | |
| | 0.30 (Γ-P)[g] | | |

[a]FP LMTO, Ref. 61.
[b]Experiment, Ref. 67.
[c]LMTO ASA, Ref. 17.
[d]LCAO, Ref. 68.
[e]VASP-PAW, Ref. 55.
[f]DMol3, Ref. 69.
[g]Experiment, Refs. 48,70.

Analysis shows that calculated effective masses for $In_2O_3$-I and -II are almost the same, while those for $In_2O_3$-III are much smaller. Hence, carrier mobility in $In_2O_3$-III is expected to be larger than that in $In_2O_3$-I and -II. The calculated effective mass for $In_2O_3$-II is much closer to experimental data than it is in ZnO. The difference in accuracy of the calculated masses comes out from strong Coulomb correlation effects, which is very strong in ZnO[55,57]. As a result, in the DFT calculations within LDA energy band of the Zn $3d$ electrons are located inappropriately close to the topmost VB, falsifying the band dispersion and, consequently, effective masses. As noted in analysis of the band dispersion [Fig. 5], In $4d$ band is located much below the topmost VB than it is in ZnO. So, Coulomb correlation effects in $In_2O_3$-I, -II, and -III are not as strong as in ZnO to falsify the band masses significantly. That is, probably, the reason why the error in effective mass values coming out from DFT calculations is much larger than $In_2O_3$-II.

### E. Charge-density and electron localization function analysis

For qualitative characterization of the bonding interaction between constituents, charge-density and electron localization function (ELF) analysis have been performed for $In_2O_3$-I [Figs. 11], -II [Figs. 12], and -III [Figs. 13]. Analysis of the charge-distribution shows that the highest charge density is residing in the immediate vicinity of the nuclei reflecting the dominant ionic type bonding. It is seen that compared to $In_2O_3$-II and -III two nearby O atoms of $In_2O_3$-I are located sufficiently closer to each other. If the bonding interaction between In and O is purely ionic one could expect negligible charge density distribution between these ions. From the Figs. 11–12 it is clear that there is finite charges distributed in between In and O in all the three polytypes. Also, the charge around In and O atoms is not distributed spherically. These features indicate that apart from dominant ionic bonding, finite covalent-like bonding interaction is present between In and O. The observed hybridization interaction is responsible for mixed nature of the electronic structure of these materials discussed in the previous section. This suggestion is confirmed by the Born effective-, Bader-, and Voronoi-charge analysis in the following section. The ELF is one of the ways of measuring the

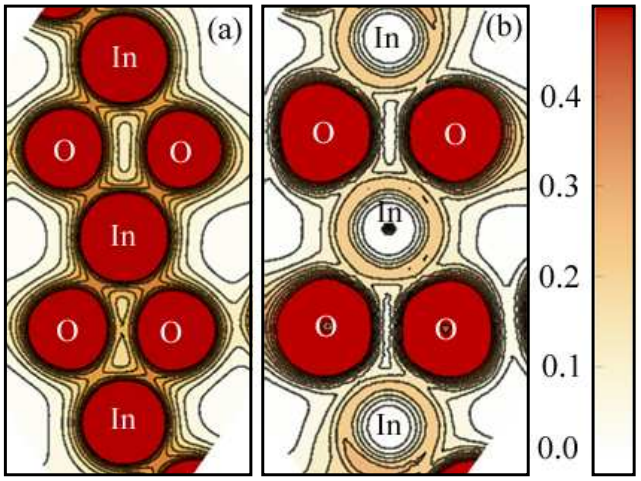


FIG. 11: (a)Charge density and (b) ELF for $In_2O_3$-I.

probability of distribution of paired electrons.[71–73] It is seen that maximum value of ELF is around O and it is low around In atoms, which confirms the dominant ionic bonding. Between the In and O atoms the ELF not show any maximum value and this indicate no dominant covalent type bonding interaction is present between these atoms. However, nonspherical distribution of ELF at the O site and small but finite value of ELF in between In

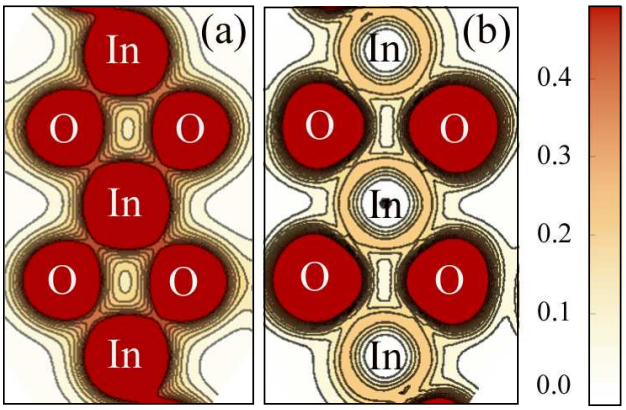


FIG. 12: (a)Charge density and (b) ELF for $In_2O_3$-II

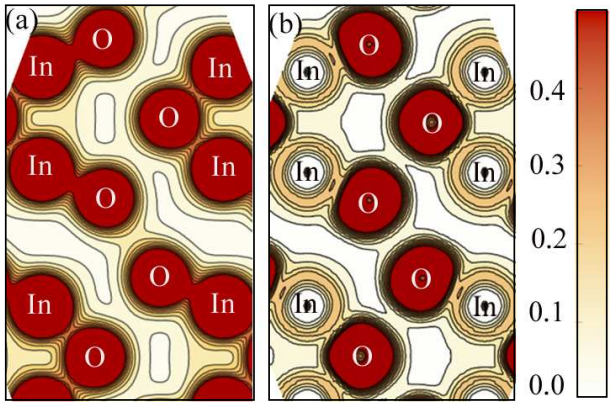


FIG. 13: (a)Charge density and (b) ELF for $In_2O_3$-III.

and O reflecting the presence nonnegligible hybridization interaction between these atoms. Unlike intermetallic phases, no isolated spot with high ELF is found in any of the $In_2O_3$ phases considered here.

### F. Bader and Voronoi charge analysis

For quantitative characterization of chemical bonding of a solid Bader and Voronoi charge analysis[74–76] are widely used. In the Bader charge analysis each atom of a compound is surrounded by a surface (called Bader regions) that run through minima of the charge density and total charge of the atom is determined by integration within the Bader region. In the Voronoi charge analysis each grid point of charge density is assigned to the nearest atom, but each of these distances are not scaled by the radius of each atom, so, the Voronoi charges in the present article is used just for a sanity check.

Table IV presents the atomic charges for $In_2O_3$-I, -II, and -III calculated according to Bader and Voronoi schemes. As expected, In atoms donate electrons, while O atoms accept them. Based on the amount of the transferred charges one can conclude that chemical bonding is of ionic type. Analysis of the Table IV shows that the charges donated by different types of In and those accepted by different O atoms of $In_2O_3$-I considerable differ from each other in agreement with orbital and site projected DOS analysis (Fig. 10 (a)).

TABLE IV: Atomic charges (in units of the electron charge $e^-$) around In and O atoms calculated according to Voronoi and Bader topological analysis for different phases of $In_2O_3$.

| Compound | Atom | Voronoi | Bader |
|---|---|---|---|
| $In_2O_3$-I | In1 | 1.75 | 1.52 |
| | In2 | 1.90 | 1.55 |
| | In3 | 1.27 | 1.48 |
| | O1 | −1.23 | −1.00 |
| | O2 | −1.38 | −1.02 |
| $In_2O_3$-II | In1 | 2.00 | 1.81 |
| | In2 | 2.04 | 1.84 |
| | O | −1.36 | −1.23 |
| $In_2O_3$-III | In | 2.09 | 1.81 |
| | O | −1.39 | −1.20 |

### G. Born effective charges

Born effective charges (BEC) are the fundamental parameters characterizing the change in electron polarization upon displacement of atoms. They are related to microscopic electron currents, produced in a system by a change of the atomic position. These currents may contribute to the BEC, which is unrelated and additional to the static electron charge carried out by the atoms during the displacement, so that BEC can be much larger than their static counterpart. In this case BEC are referred to as anomalous. BEC are the important parameters, which are helpful to understand ferroelectric and piezoelectric properties of materials. We have calculated BEC for $In_2O_3$-III. The results are presented in Table V. The charge of the nucleus and the core electrons included into the pseudopotentials is three for In and six for O atoms. It is seen that for In atoms non diagonal elements of the BEC tensor is negligible compared to diagonal elements. It shows that In atoms donate electrons only to the six nearest neighbor O atoms, but there is no electronic exchange with other In or next nearest neighbor O atoms and the chemical bonding is ionic. However, non diagonal elements of BEC of the O atoms are comparable with those of diagonal elements. Since the In–O bond is ionic, one can expect that the O atoms form chemical bonding not only with the nearest neighbor In atoms, but, probably, with second nearest neighbor O atoms also. This result is in agreement with charge density and ELF analysis [Fig. 13], which demonstrates that there is chemical bonding between two nearest neighbor O atoms.

BEC have not been calculated for $In_2O_3$-I and -II. However, based on previous studies one can make some suggestions about BEC in these phases of $In_2O_3$. One of the important questions in point is how BEC is sensitive to crystal structures. In experimental studies of BEC for $KNbO_3$ (Ref. 77) and $PbTiO_3$ (Ref. 78) it was

TABLE V: Calculated Born-effective-charge-tensor elements ($Z^*$) for the constituents of $In_2O_3$-III.

| Atom | $xx$ | $yy$ | $zz$ | $xy$ | $yz$ | $zx$ | $xz$ | $zy$ | $yx$ |
|---|---|---|---|---|---|---|---|---|---|
| In1 | 3.300 | 3.306 | 3.206 | 0.009 | 0.002 | 0.000 | 0.001 | 0.000 | 0.002 |
| O1 | -2.260 | -2.136 | -2.130 | 0.098 | 0.432 | 0.186 | 0.257 | 0.308 | 0.432 |

concluded that the BEC are insensitive to crystal structure. However, this point was argued in Ref. 79 and it was shown that cubic $BaTiO_3$ posses highest value of BEC, which decreased if one moves from cubic to tetragonal, orthorhombic, and rhombohedral lattices. Since BEC is closely related to orbital hybridizations, they are expected to be influenced by structural phase transitions. Based on the result one can say that BEC for cubic $In_2O_3$-I and -II are expected to be higher than those for $In_2O_3$-III. Furthermore, as it follows from charge density and ELF analysis, there is no chemical bonding between two nearest neighbor O atoms of $In_2O_3$-I and -II. So in the phases one can expect almost zero non-diagonal elements of BEC.

It is seen that the charges around In and O atoms are slightly larger than those in a pure ionic picture: they show significant contribution of the dynamic charge to the static charge and the BEC can not be said to be anomalous.

### H. Optical properties

The calculated optical spectra for all the three polytypes of indium oxides are presented in Fig. 14. The real and imaginary part of the optical dielectric response function, absorption coefficient and reflectivity, as well as the refractive index and the extinction coefficient have been analyzed. Since crystal structures of $In_2O_3$-I and -II are cubic, optical spectra are isotropic along the crystallographic $a, b$ and $c$ axes. So, only one of the components is sufficient for the analysis. All the optical spectra of $In_2O_3$-I, -II, and -III are shifted toward lower energies owing to the underestimation of the band gap in the DFT calculations. For $In_2O_3$-I the shift toward lower energies is much more severe compared to $In_2O_3$-II and -III. One of the ways to correct the DFT error is to use the scissors operator technique, i.e. rigid shift of all the CB states, so that the optical spectra shall also be shifted accordingly.[56,65,66,80] The search of literature shows that among $In_2O_3$-I and -II experimental data is available for the latter in Ref. 48, where reflectivity and transmittance spectra were measured by spectrophotometry at room temperature. The other optical spectra such as absorption coefficient, refractive index, and the extinction coefficient are calculated using the Kramers–Kronig relation. These five optical spectra have been compared in Fig. 14 (a) with those calculated from the present band structure results. It should be noted that the optical spectra of $In_2O_3$-II in Ref. 48 were measured for the energy range 0–6 eV, those contain only the $E_0$ peak induced by electronic transitions from the VB maximum to CB minimum occurring at the Γ point. So, in the present work these experimental data were used only for rigid shift of the calculated optical spectra toward higher energies by 1.65 eV to fit to location of the $E_0$ peak. Since the location of the $E_0$ peak is clearly seen in the spectra of $n(\omega)$, fitting was performed for $n(\omega)$. The other spectra have been shifted accordingly. Optical spectra of $In_2O_3$-I have also been shifted by 1.65 eV to higher energies based on its similarity of basic peaks to that of $In_2O_3$-II. To know whether the rigid shift technique can be applied or not for a particular compound, one needs measured optical spectra for wider energy range, which contains more basic peaks in the optical spectra. Currently there are no such experimental data available for these compounds. So, in the present paper it is assumed that the rigid shift technique can be applied.

From the comparison of the calculated spectra with experimentally measured spectra one can see that the calculated $n(\omega)$ and $k(\omega)$ agree well with experimental data. Calculated reflectivity spectra agrees with experimental data only at higher energies well above the band gap. At lower energies, below the band gap, experimental reflectivity is higher than that calculated by DFT and this peak may be associated with excitonic effect which is not considered in the present calculations. Measured absorption spectra agrees with calculated one at lower energies. At energies exceeding the location of the $E_0$ peak, the experimentally determined absorption spectra exceeds the calculated values.

Analysis of Fig. 14 shows that optical spectra of $In_2O_3$-I oscillate unusually in the energy range 0.0–7.5 eV, which, probably, is related to severe underestimation of the band gap of $In_2O_3$-I in the DFT calculations. The Coulomb correlation effects from In $4d$ electrons may be important for this case to describe the optical properties correctly. Calculation of optical properties by including orbital dependent potential into the calculation is necessary to clarify this issue. Only at higher energy range 7.5–20.0 eV the optical spectra of $In_2O_3$-I and -II are somewhat closer to each other although the optical spectra of the former is systematically smaller than the latter.

Since the optical spectra are obtained from the interband transitions, the origin of the peaks can be explained through the band structure. Following the analogy with notations used in Ref. 42 for reflectivity spectra of semiconductors with zinc blende structure, the $E_0, E_1$, and $E_2$ peaks of $In_2O_3$-I and -II originate from optical transitions from VB maximum to CB minimum occurring at Γ-point for the $E_0$ peak, $H$ and $P$ points for the $E_1$ peak, and the $N$ point for the $E_2$ peak. $d_1$ and $d_2$ peaks are, probably, originated from optical transitions from the In $4d$ states.

Because of the rhombohedral symmetry, there is optical anisotropy present in $In_2O_3$-III. The two components of the dielectric functions are calculated for $In_2O_3$-III corresponding to the electric field parallel $E \parallel c$ and perpen-

dicular $E \perp c$ to the crystallographic $c$ axes. The first experimental data for $In_2O_3$-III is already available.[11] The absorption coefficient was measured for the energy range 0–6 eV, which contain the $E_0$ peak. Calculated absorption spectra was shifted to 1.35 eV toward higher energies to fit the $E_0$ peak to experimentally determined location. The other optical spectra have been shifted accordingly. It is seen that after the scissor operation the calculated $E_0$ peak intensity is comparable with the experimentally measured one.

The origin of the $E_0, E_1$ and $E_2$ peaks can be explained following the analogy with the notation used in Ref. 42 for wurtzite semiconductors. The direct optical transition from VB maximum to CB minimum located at the Γ-point is responsible for the $E_0$ peak, $Z$ and $L$ points are responsible for $E_1$ peak $E_2$ peaks, respectively. $d_1$ and $d_2$ peaks located at energies >10 eV are, probably, caused by optical transitions from the In $4d$ states.

The anisotropy is well pronounced at energies from 7 to 9 eV, whereas the optical spectra are more or less isotropic at other energies considered. Location of the all major peaks of the optical spectra corresponding to both of the directions are the same. However, magnitudes of the peaks along the two directions coincide only in the energy ranges 0–7 eV and 8.5–20.0 eV. In the range 7.0–8.5 eV, magnitude of the $E_2$ peak for $E \parallel c$ at around 7.5 eV and its shoulder at 8.3 eV are larger than those for $E \perp c$. Absorption and reflectivity spectra for this compound is also low in the energy range 0–5 eV.

As discussed above, the intensity of the calculated optical spectra are differ from experimentally measured one for both $In_2O_3$-II and -III. The reason of this deviation can be related to overestimation of the momentum matrix elements, neglect of the Coulomb interaction between free electrons and holes (excitons), local-field and finite lifetime effects. Furthermore, in the calculations of the imaginary part of the dielectric response function direct optical transitions from occupied to unoccupied states are only considered only. Also, charge fluctuations and the experimental resolution smears out many fine features. Based on analysis of the optical spectra of $In_2O_3$-I, -II, and -III one can say that $In_2O_3$-II and -III can be considered as potential candidates for transparent oxides.

## IV. CONCLUSION

Structural properties, electronic structure, high-pressure behavior, and optical properties of $In_2O_3$ of space group symmetry $I2_13, Ia\bar{3}$ and $R\bar{3}$ are studied by DFT calculations. From studies of structural properties of $In_2O_3$ lattice and positional parameters have been found, which are in good agreement with experimental data. Pressure-induced phase transition is shown to be possible from $In_2O_3$-I to -III and from $In_2O_3$-II to -III. Transition pressure values have been calculated. Based on the analysis of band structure it is found that $In_2O_3$-I is indirect band gap, while that of $In_2O_3$-II is direct band gap. Optical gap of $In_2O_3$-III is found to be larger than that of $In_2O_3$-II. Intermediate band is found in $In_2O_3$-I located right up the Fermi energy. The band is isolated from the valence and conduction bands. From orbital decomposition analysis, and orbital and site projects density of states nature of the valence and conduction bands have been determined. It is shown that the topmost valence band consists of O $2p$ states hybridized with In $4d$ states. It is found that the intermediate band minimum of $In_2O_3$-I is of O $2p$ character hybridized with In $5s$ and $4d$ orbitals. Conduction band minimum of $In_2O_3$-II and -III consist of In $5s$ orbitals. By orbital and site decomposition of bands it is shown that the topmost valence band of $In_2O_3$-I, -II, and -III is contributed from O $2p_x, 2p_y, 2p_z$ slightly hybridized with In $4d_{xy}, 4d_{xz}, 4d_{yz}$. Intermediate band minimum of $In_2O_3$-I is found to be contributed from O $2p_x, 2p_y$ and $2p_z$ orbitals hybridized with In $5s$ and In $4d_{xy}, 4d_{xz}, 4d_{yz}$. Conduction band minimum of $In_2O_3$-II consists of In $5s$ orbitals hybridized with O $2s$. Conduction band effective masses are found to be almost isotropic. From charge-density, electron localization function, Bader, and Voronoi charge analysis it is found that the $In_2O_3$ phases considered are more ionic. Magnitude of the absorption and reflection coefficients of $In_2O_3$ with space group $Ia\bar{3}$ and $R\bar{3}$ are small in the energy range 0-5 eV, so that these materials can re regarded and classified as transparent.

### Acknowledgments

This work has been supported by FUNMAT under the project number 101043 and supercomputing support through the Research Council of Norway. The authors gratefully acknowledge Dr. Ch. Y. Wang (Institute of Micro- and Nanotechnologies, Technical University Ilmenau, Ilmenau, Germany) for fruitful discussions and sending experimental data used for comparison with the the theoretical results of the present work. We are thankful to Dr. R. Vidya and A. Klaveness for help in plotting figures and discussions.

[1] H. Kawazoe, M. Yasukawa, H. Hyodo, M. Kurita, H. Yanagi, and H. Hosono, Lett. Nature **389**, 939 (1997).
[2] G. Thomas, Nature **389**, 907 (1997).
[3] H. Sato, T. Minami, S. Takata, and T. Yamada, Thin Solid Films **236**, 27 (1993).
[4] J. F. Wager, Science **300**, 1245 (2003).
[5] A. N. Banerjee and K. K. Chattopadhyay, Progress in Crystal Growth and Characterization of Mater. **50**, 528 (2006).
[6] R. Martins, E. Fortunato, P. Nunes, I. Ferreira, A. Mar-

ques, M. Bender, N. Katsarakis, V. Cimalla, and G. Kiriakidis, J. Appl. Phys. **96**, 1398 (2004).
[7] A. V. Mudryi, A. V. Ivaniukovich, and A. G. Ulyashin, Thin SOlid Films **Accepted for publication** (2006).
[8] W. Zachariasen, Norsk Geologisk Tidsskrift **9**, 310 (1927).
[9] I. Tanaka, M. Mizuno, and H. Adachi, Phys. Rev. B **56**, 3536 (1997).
[10] M. Sorescu, L. Diamandescu, D. Tarabasanu-Mihaila, and V. S. Teodorescu, J. Mater. Sci. **39**, 675 (2004).
[11] C. Y. Wang, V. Cimalla, H. Romanus, T. Kups, G. Ecke, T. Stauden, M. Ali, V. Lebedev, J. Pezoldt, and O. Ambacher, Appl. Phys. Lett. **89**, 011904 (2006).
[12] B. Yaglioglu, H.-Y. Yeom, and D. Paine, Appl. Phys. Lett. **86**, 261908 (2005).
[13] C. Warmsingh, Y. Yoshida, D. W. Readey, C. W. Teplin, J. D. Perkins, P. A. Parilla, L. M. Gedvilas, B. M. Keyes, and D. S. Ginley, J. Appl. Phys. **95**, 3831 (2004).
[14] M. F. A. M. van Hest, M. S. Dabney, J. D. Perkins, D. S. Ginley, and M. P. Taylor, Appl. Phys. Lett. **87**, 032111 (2005).
[15] T. Koida and M. Kondo, J. Appl. Phys. **99**, 123703 (2006).
[16] Y. Mi, H. Odaka, and S. Iwata, Jpn. J. Appl. Phys. **38**, 3453 (1999).
[17] H. Odaka, S. Iwata, N. Taga, S. Ohnishi, Y. Kaneta, and Y. Shigesato, Jpn. J. Appl. Phys. **36**, 5551 (1997).
[18] O. N. Mryasov and A. J. Freeman, Phys. Rev. B **64**, 233111 (2001).
[19] A. J. Freeman, K. R. Poeppelmeier, T. O. Mason, R. Chang, and T. J. Marks, MRS Bulletin **25**, 45 (2000).
[20] L. A. Errico, M. Rentería, G. Fabricius, and G. N. Darriba, Hyperfine interact. **158**, 63 (2005).
[21] T. Tomita, K. Yamashita, Y. Hayafuji, and H. Adachi, Appl. Phys. Lett. **87**, 05 1911 (2005).
[22] J. C. C. Fan and J. B. Goodenough, J. Appl. Phys. **48**, 3524 (1977).
[23] S. A. Knickerbocker and A. K. Kulkarni, J. Vac. Sci. Technol. **13**, 1048 (1995).
[24] A. K. Kulkarni and S. A. Knickerbocker, J. Vac. Sci. Technol. **14**, 1709 (1996).
[25] A. K. Kulkarni and S. A. Knickerbocker, J. Vac. Sci. Technol. **14**, 757 (1996).
[26] C.-Y. Ren, S.-H. Chiou, and J. Choisnet, J. Appl. Phys. **99**, 02 3706 (2006).
[27] *Inorganic Crystal Structure Database* (Gmelin Institut, Karlsruhe, 2001).
[28] M. Marezio, Acta Cryst. **20**, 723 (1966).
[29] C. T. Prewitt, R. D. Shaxnon, D. B. Rogers, and A. W. Sleight, Inorg. Chem. **8**, 1985 (1969).
[30] G. Kresse and J. Furthmüller, Phys. Rev. B **54**, 11 169 (1996).
[31] P. Hohenberg and W. Kohn, Phys. Rev. **136**, B864 (1964).
[32] W. Kohn and L. J. Sham, Phys. Rev. **140**, A1133 (1965).
[33] J. P. Perdew and A. Zunger, Phys. Rev. B **23**, 5048 (1981).
[34] D. M. Ceperley and B. J. Alder, Phys. Rev. Lett. **45**, 566 (1980).
[35] P. E. Blöchl, Phys. Rev. B **50**, 17 953 (1994).
[36] G. Kresse and D. Joubert, Phys. Rev. B **59**, 1758 (1999).
[37] B. Adolph, J. Furthmüller, and F. Bechstedt, Phys. Rev. B **63**, 12 5108 (2001).
[38] P. Ravindran, A. Delin, R. Ahuja, B. Johansson, S. Auluck, J. Wills, and O. Eriksson, Phys. Rev. B **56**, 6851 (1997).
[39] P. Ravindran, A. Delin, P. James, B. Johansson, J. Wills, R. Ahuja, and O. Eriksson, Phys. Rev. B **59**, 15 680 (1999).
[40] P. Ravindran, A. Delin, B. Johansson, O. Eriksson, and J. Wills, Phys. Rev. B **59**, 1176 (1999).
[41] A. Delin, P. Ravindran, O. Eriksson, and J. Wills, Int. J. Quantum Chem. **69**, 349 (1998).
[42] M. Cardona and G. Harbeke, Phys. Rev. **137**, A1467 (1965).
[43] P. Vajeeston, P. Ravindran, A. Kjekshus, and H. Fjellvåg, J. Alloys Compd. **363**, L7 (2004).
[44] P. Vajeeston, P. Ravindran, A. Kjekshus, and H. Fjellvåg, Phys. Rev. B **71**, 09 2103 (2005).
[45] R. D. Shannon, Solid State Commun. **4**, 629 (1966).
[46] H. R. Hoekstra, Inorg. Chem. **5**, 754 (1966).
[47] T. Wittkowski, J. Jorzick, H. Seitz, B. Schröder, K. Jung, and B. Hillebrands, Thin Solid Films **398–399**, 465 (2001).
[48] I. Hamberg, C. G. Grandqvist, K. F. Berggren, B. E. Sernelius, and L. Engström, Phys. Rev. B **30**, 3240 (1984).
[49] R. L. Weiher and R. P. Ley, J. Appl. Phys. **37**, 299 (1966).
[50] M. Anwar, I. M. Ghauri, and S. A. Siddiqi, J. Mater. Sci. **41**, 2859 (2006).
[51] J. E. Medvedeva, arXiv:cond-mat/0605443 **2**, 1 (2006).
[52] M. Orita, H. Sakai, M. Takeuchi, Y. Yamaguchi, T. Fujimoto, N. Fukumoto, and I. Kojima, J. Surf. Sci. Soc. Jpn., Hyomen Kagaku **17**, 440 (1996).
[53] T. Barr and Y. L. Liu, J. Phys. Chem. Solids **50**, 657 (1989).
[54] C. McGuinness, C. B. Stagarescu, P. J. Ryan, J. E. Downes, D. Fu, K. E. Smith, and R. G. Egdell, Phys. Rev. B **68**, 16 5104 (2003).
[55] S. Z. Karazhanov, P. Ravindran, U. Grossner, A. Kjekshus, H. Fjellvåg, and B. G. Svensson, J. Appl. Phys. **100**, 04 3709 (2006).
[56] S. Lalitha, S. Z. Karazhanov, P. Ravindran, S. Senthilarasu, R. Sathyamoorthy, and J. Janabergenov, Phys. B **387**, 227(2006).
[57] S. Z. Karazhanov, P. Ravindran, U. Grossner, A. Kjekshus, H. Fjellvåg, and B. G. Svensson, Solid State Commun. **139**, 391 (2006).
[58] S. Z. Karazhanov, P. Ravindran, P. Vajeeston, A. Ulyashin, H. Fjellvåg, and B. G. Svensson, To be published (2006).
[59] Y. Furubayashi, T. Hitosugi, Y. Yamamoto, Y. Hirose, G. Kinoda, K. Inaba, T. Shimada, and T. Hasegawa, Thin Solid Films **496**, 157 (2006).
[60] R. Asahi, Y. Taga, W. Mannstadt, and A. J. Freeman, Phys. Rev. B **61**, 7459 (2000).
[61] W. R. L. Lambrecht, A. V. Rodina, S. Limpijumnong, B. Segall, and B. K. Meyer, Phys. Rev. B **65**, 07 5207 (2002).
[62] W. R. L. Lambrecht and B. Segall, Phys. Rev. B **52**, R2249 (1995).
[63] K. Kim, W. R. L. Lambrecht, B. Segall, and M. Schilfgaarde, Phys. Rev. B **56**, 7363 (1997).
[64] S. Z. Karazhanov and L. C. Lew Yan Voon, Semicond **39**, 177 (2005).
[65] L. C. Lew Yan Voon, M. Willatzen, and M. Cardona, Phys. Rev. B **53**, 10 703 (1996).
[66] M. Willatzen, M. Cardona, and N. E. Christensen, Phys. Rev. B **51**, 17 992 (1995).
[67] K. Hümmer, Phys. Status Solidi **B 56**, 249 (1973).
[68] Y.-N. Xu and W. Y. Ching, Phys. Rev. B **48**, 4335 (1993).
[69] S. H. Brewer and S. Franzen, Chem. Phys. **300**, 285 (2004).
[70] Y. Ohhata, F. Shinoki, and S. Yoshida, Thin Solid Films **59**, 255 (1979).
[71] P. Vajeeston, P. Ravindran, R. Vidya, A. Kjekshus, and H. Fjellvåg, Europhys. Lett. **72**, 569 (2005).

[72] A. D. Becke and K. E. Edgecombe, J. Chem. Phys. **92**, 5397 (1990).

[73] B. Silvi and A. Savin, Nature **371**, 683 (2004).

[74] R. F. W. Bader, *Atoms in molecules: A Quantum Theory* (Oxford University Press, New York, 1990).

[75] G. Henkelman, A. Arnaldsson, and H. Jónsson, Comput. Mater. Sci. **36**, 354 (2006).

[76] C. F. Guerra, J.-W. Handgraaf, E. J. Baerends, and F. M. Bickelhaupt, J. Comput. Chem. **25**, 189 (2003).

[77] R. Resta, M. Posternak, and A. Baldereschi, Phys. Rev. Lett. **70**, 1010 (1993).

[78] L. Canali1, M. Lazzarino, L. Sorba, and F. Beltram, Phys. Rev. Lett. **72**, 3618 (1993).

[79] P. Ghosez, X. Gonze, P. Lambin, and J. P. Michenaud, Phys. Rev. B **51**, 6765 (1995).

[80] W. R. L. Lambrecht, B. Segall, J. Rife, W. R. Hunter, and D. K. Wickenden, Phys. Rev. B **51**, 13 516 (1995).


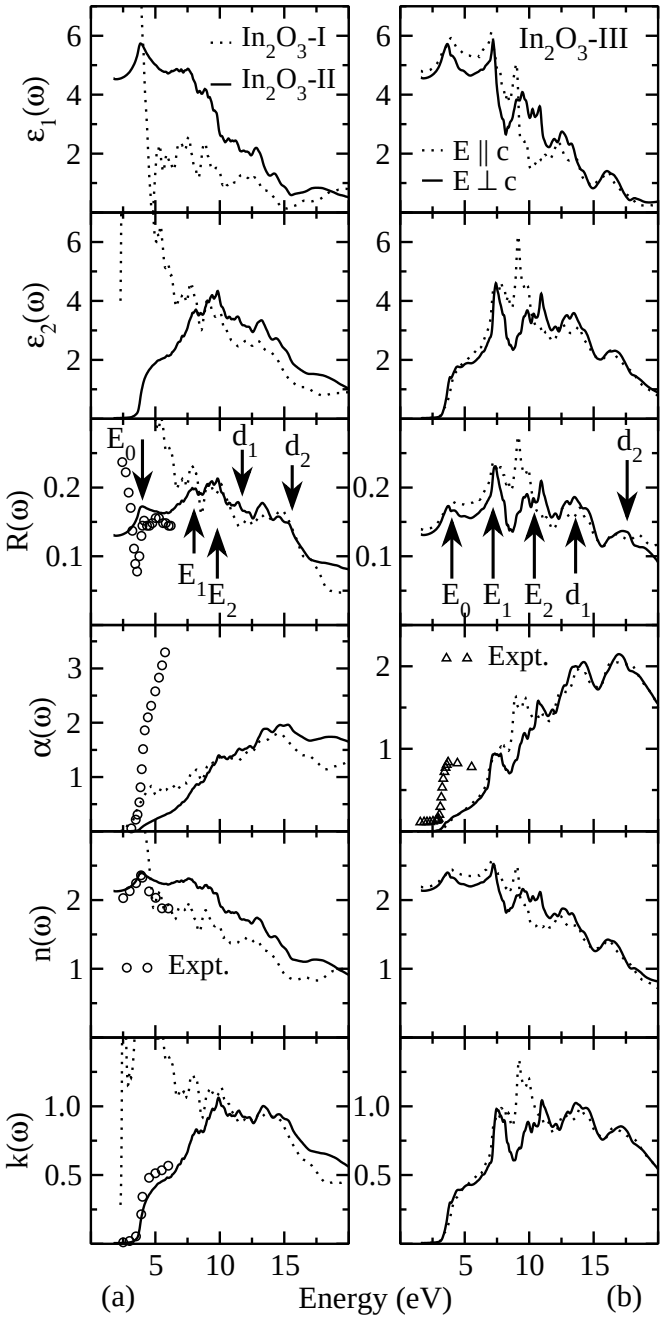


FIG. 14: Optical spectra of (a) $In_2O_3$-I and $In_2O_3$-II, and (b) $In_2O_3$-III for directions of the electric field ($E$) parallel ($E \parallel c$) and perpendicular ($E \perp c$) to the crystallographic $c$ axes. Calculated absorption coefficient, reflectivity, refractive index, and extinction coefficients for (a) $In_2O_3$-II have been compared with experimental data of Ref. 48. Calculated absorption coefficient for (b) $In_2O_3$-III has been compared with experimental results of Ref. 11. The absorption coefficients are given in [$cm^{-1}$] divided by $10^5$.